



IMPORTANCE OF ALIGNING TRAINING STRATEGY WITH EVALUATION FOR DIFFUSION MODELS IN 3D MULTICLASS SEGMENTATION

A PREPRINT

 **Yunguan Fu**  **Yiwen Li**  **Shaheer U. Saeed**  **Matthew J. Clarkson**
University College London University of Oxford University College London University College London
InstaDeep

 **Yipeng Hu**
University College London
University of Oxford

ABSTRACT

Recently, denoising diffusion probabilistic models (DDPM) have been applied to image segmentation by generating segmentation masks conditioned on images, while the applications were mainly limited to 2D networks without exploiting potential benefits from the 3D formulation. In this work, for the first time, DDPMs are used for 3D multiclass image segmentation. We make three key contributions that all focus on aligning the training strategy with the evaluation methodology, and improving efficiency. Firstly, the model predicts segmentation masks instead of sampled noise and is optimised directly via Dice loss. Secondly, the predicted mask in the previous time step is recycled to generate noise-corrupted masks to reduce information leakage. Finally, the diffusion process during training was reduced to five steps, the same as the evaluation. Through studies on two large multiclass data sets (prostate MR and abdominal CT), we demonstrated significantly improved performance compared to existing DDPMs, and reached competitive performance with non-diffusion segmentation models, based on U-net, within the same compute budget. The JAX-based diffusion framework has been released on <https://github.com/mathpluscode/ImgX-DiffSeg>.

Keywords Image Segmentation · Diffusion Model · Prostate MR · Abdominal CT

1 Introduction

Multiclass segmentation is one of the most basic tasks in medical imaging, one that arguably benefited the most from deep learning. Although different model architectures [Li et al., 2021, Strudel et al., 2021] and training strategies [Cheplygina et al., 2019, Fu et al., 2019, Li et al., 2022] have been proposed for specific clinical applications, U-net [Ronneberger et al., 2015] trained through supervised training remains the state-of-the-art and an important baseline for many [Ji et al., 2022]. Recently, denoising diffusion probabilistic models (DDPM) have been demonstrated to be effective in a variety of image synthesis tasks [Ho et al., 2020], which can be further guided by a scoring model to generate conditioned images [Dhariwal and Nichol, 2021] or additional inputs [Ho and Salimans, 2022]. These generative modelling results are followed by image segmentation, where the model generates segmentation masks by progressive denoising from random noise. During training, DDPM is provided with an image and a noise-corrupted segmentation mask, generated by a linear interpolation between the ground-truth and a sampled noise. The model is then tasked to predict the sampled noise [Amit et al., 2021, Kolbeinsson and Mikolajczyk, 2022, Wolleb et al., 2022, Wu et al., 2022] or the ground-truth mask [Chen et al., 2022].

However, existing applications have all been based on 2D networks and, for 3D volumetric medical images, slices are segmented before obtaining the assembled 3D segmentation. Challenges are often encountered for 3D images.

Firstly, the diffusion model requires image and noise-corrupted masks as input, requiring an increased memory footprint resulting in limited batch size and potentially excessive training time. Second, most diffusion models assume a denoising process of hundreds of time steps for training and inference, the latter of which in particular leads to prohibitive inference time (e.g., days on TPUs/GPUs).

This work addresses these issues by investigating an overarching strategy that aligns training with evaluation processes, including: **1)** Directly predicting ground-truth masks instead of sampled noise. This facilitates the direct use of Dice loss in addition to cross-entropy during training, as opposed to existing work that uses L_2 loss on noise. Although debatable, Dice is the most reported segmentation metric at inference. **2)** As discussed in multiple studies [Chen et al., 2022, Young et al., 2022, Kolbeinsson and Mikolajczyk, 2022], morphological features may be preserved in noise-corrupted masks during training. Therefore, model predictions are recycled during training to avoid leakage and better “emulate” the evaluation process. **3)** Instead of denoising with at least hundreds of steps as in most existing work, we propose a five-step denoising process for both training and inference, resorting to resampling variance scheduling [Nichol and Dhariwal, 2021]. With extensive experiments in two of the largest public multiclass segmentation applications, prostate MR (589 images) and abdominal CT images (300 images) [Li et al., 2022, Ji et al., 2022], we

- Propose the first 3D network-based DDPMs for volumetric image segmentation that yields significantly improved performance, compared to existing 2D DDPMs, and competitive performance, compared to non-diffusion supervised learning, using the same computational cost.
- Demonstrate that reducing the discrepancy between training and evaluation processes is effective for improving training efficiency and model performance.

We also release the first unit-tested JAX-based diffusion segmentation framework, with both 2D and 3D networks. The code has been anonymised and released on <https://github.com/mathpluscode/ImgX-DiffSeg>.

2 Related Work

The diffusion probabilistic model was first proposed by Sohl-Dickstein et al. [2015] as a generative model for image sampling with a forward noising process. Ho et al. [2020] proposed a reverse denoising process that estimates the sampled error, achieving state-of-the-art performance in unconditioned image synthesis at the time. Different conditioning methods were later proposed to guide the sampling process toward a desired image class or prompt text, using gradients from an external scoring model [Dhariwal and Nichol, 2021, Radford et al., 2021]. Alternatively, Ho and Salimans [2022] showed that guided sampling can be achieved by providing conditions during training. Diffusion models have been successfully applied in medical imaging applications to synthesise images of different modalities, such as unconditioned lung X-Ray and CT [Ali et al., 2023], patient-conditioned brain MR [Pinaya et al., 2022], temporal cardiac MR [Kim and Ye, 2022], and pathology/sequence-conditioned prostate MR [Saeed et al., 2023]. The synthesised images have been shown to benefit pre-training self-supervised models [Khader et al., 2022, Saeed et al., 2023] or support semi-supervised learning [Young et al., 2022].

Besides image synthesis, Baranchuk et al. [2021] used pre-trained diffusion models’ intermediate feature maps to train pixel classifiers for segmentation, showing these unsupervised models capture semantics that can be extended for image segmentation especially when training data is limited. Alternatively, Amit et al. [2021] performed progressive denoising from random sampled noise to generate segmentation masks instead of images for microscopic images [Amit et al., 2021]. At each step, the model takes a noise-corrupted mask and an image as input and predicts the sampled noise. Similar approaches have been also applied to thyroid lesion segmentation for ultrasound images [Wu et al., 2022] and brain tumour segmentation for MR images with different network architectures [Wolleb et al., 2022, Wu et al., 2022]. Empirically, multiple studies [Chen et al., 2022, Young et al., 2022, Kolbeinsson and Mikolajczyk, 2022] found the noise-corrupted mask generation, via linear interpolation between ground-truth masks and noise, retained morphological features during training, causing potential data leakage. Chen et al. [2022] therefore added noises to mask analog bit and tuned its scaling. Young et al. [2022], on the other hand, tuned the variance and scaling of added normal noise to reduce information contained in noised masks. Furthermore, Kolbeinsson and Mikolajczyk [2022] proposed recursive denoising instead of directly using ground truth for noise-corrupted mask generation.

These works, although using different methods, are all addressing a similar concern: the diffusion model training process is different from its evaluation process, which potentially hinders the efficient learning. Moreover, all published diffusion-model-based segmentation applications have been based on 2D networks. We believe such discrepancy would be more significant when applying 3D networks to volumetric images due to the increased difficulty, resulting in longer training and larger compute cost. In this work, building on these recent developments, we focus on a consistent train-evaluate algorithm for efficient training of diffusion models in 3D medical image segmentation applications.

3 Method

3.1 DDPM with Variance Schedule Resampling

Model The denoising diffusion probabilistic models (DDPM) [Sohl-Dickstein et al., 2015, Ho et al., 2020, Nichol and Dhariwal, 2021, Kingma et al., 2021] consider a *forward* process: given a data point $\mathbf{x}_0 \sim q(\mathbf{x}_0)$, noise is added to \mathbf{x}_t for $t = 1, \dots, T$ with multivariate normal distribution, $q(\mathbf{x}_t | \mathbf{x}_{t-1}) = \mathcal{N}(\mathbf{x}_t; \sqrt{1 - \beta_t}\mathbf{x}_{t-1}, \beta_t \mathbf{I})$, where $\beta_t \in [0, 1]$ is a variance schedule. Given a sufficiently large T , \mathbf{x}_T approximately follows an isotropic multivariate normal distribution $\mathcal{N}(\mathbf{x}_T; \mathbf{0}, \mathbf{I})$. A *reverse* process is then defined to denoise \mathbf{x}_t at each step, for $t = T, \dots, 1$, $p_\theta(\mathbf{x}_{t-1} | \mathbf{x}_t) = \mathcal{N}(\mathbf{x}_{t-1}; \boldsymbol{\mu}_\theta(\mathbf{x}_t, t), \sigma_t^2 \mathbf{I})$, with a predicted mean $\boldsymbol{\mu}_\theta(\mathbf{x}_t, t)$ and a variance schedule $\sigma_t^2 \mathbf{I}$.

Training In practise, σ_t^2 is set to β_t or $\tilde{\beta}_t = \frac{1 - \bar{\alpha}_{t-1}}{1 - \bar{\alpha}_t} \beta_t$, where $\alpha_t = 1 - \beta_t$, $\bar{\alpha}_t = \prod_{s=0}^t \alpha_s$ and the loss is, depending on the intended model prediction,

$$L_{\text{simple}, \epsilon_t}(\theta) = \mathbb{E}_{t, \mathbf{x}_0, \epsilon_t} \|\epsilon_t - \epsilon_{t, \theta}(\mathbf{x}_t(\mathbf{x}_0, \epsilon_t), t)\|_2^2, \quad (\text{Predict } \epsilon_t) \quad (1)$$

$$L_{\text{simple}, \mathbf{x}_0}(\theta) = \mathbb{E}_{t, \mathbf{x}_0, \epsilon_t} \|\mathbf{x}_0 - \mathbf{x}_{0, \theta}(\mathbf{x}_t(\mathbf{x}_0, \epsilon_t), t)\|_2^2. \quad (\text{Predict } \mathbf{x}_0) \quad (2)$$

with t sampled from 1 to T , $\epsilon_t \sim \mathcal{N}(\mathbf{0}, \mathbf{I})$, and $\mathbf{x}_t(\mathbf{x}_0, \epsilon_t) = \sqrt{\bar{\alpha}_t}\mathbf{x}_0 + \sqrt{1 - \bar{\alpha}_t}\epsilon_t$.

Inference During inference, the generative process starts with normal noise $\mathbf{x}_T \sim \mathcal{N}(\mathbf{0}, \mathbf{I})$. At each step $\mathbf{x}_{t_{k-1}}$ is then sampled with the predicted mean $\boldsymbol{\mu}_\theta$,

$$p_\theta(\mathbf{x}_{t-1} | \mathbf{x}_t) = \mathcal{N}(\mathbf{x}_{t-1}; \boldsymbol{\mu}_\theta(\mathbf{x}_t, t), \sigma_t^2 \mathbf{I}), \quad (3)$$

$$\boldsymbol{\mu}_\theta(\mathbf{x}_t, t) = \frac{1}{\sqrt{\alpha_t}}(\mathbf{x}_t - \frac{\beta_t}{\sqrt{1 - \bar{\alpha}_t}}\epsilon_{t, \theta}(\mathbf{x}_t, t)), \quad (\text{Predict } \epsilon_t) \quad (4)$$

$$\boldsymbol{\mu}_\theta(\mathbf{x}_t, t) = \frac{\sqrt{\bar{\alpha}_{t-1}}\beta_t}{1 - \bar{\alpha}_t}\mathbf{x}_{0, \theta}(\mathbf{x}_t, t) + \frac{1 - \bar{\alpha}_{t-1}}{1 - \bar{\alpha}_t}\sqrt{\alpha_t}\mathbf{x}_t. \quad (\text{Predict } \mathbf{x}_0) \quad (5)$$

Variance sampling During training or inference, given a variance schedule $\{\beta_t\}_{t=1}^T$, a subsequence $\{\beta_k\}_{k=1}^K$ can be sampled with $\{t_k\}_{k=1}^K$, where $t_K = T$, $t_1 = 1$, $\beta_k = 1 - \frac{\bar{\alpha}_{t_k}}{\bar{\alpha}_{t_{k-1}}}$, $\tilde{\beta}_k = \frac{1 - \bar{\alpha}_{t_k-1}}{1 - \bar{\alpha}_{t_k}}\beta_{t_k}$. α_k and $\bar{\alpha}_k$ were recalculated correspondingly.

3.2 Diffusion Model for Segmentation

Training The previously applied DDPMs for image segmentation [Amit et al., 2021, Wu et al., 2022] (Fig. 1) predict noise $\epsilon_{t, \theta}$ given noised mask \mathbf{x}_t , time t , and image I . The models were trained using L_2 loss between predicted and sampled noises:

$$L_{\text{seg}, \epsilon_t}(\theta) = \mathbb{E}_{t, \mathbf{x}_0, \epsilon_t, I} \|\epsilon_t - \epsilon_{t, \theta}(\mathbf{x}_t, t, I)\|_2^2, \quad (6)$$

A segmentation-specific loss, such as Dice loss or cross-entropy loss, can also be defined between the predicted and ground-truth masks:

$$L_{\text{seg}, \mathbf{x}_0}(\theta) = \mathbb{E}_{t, \mathbf{x}_0, \epsilon_t, I} \mathcal{L}_{\text{seg}}(\mathbf{x}_0, \mathbf{x}_{0, \theta}(\mathbf{x}_t, t, I)), \quad (7)$$

where $\mathbf{x}_{0, \theta}$ can be predicted by the model or derived from predicted noise.

Inference Inference is the same as in Section 3.1 with additional input I .

Recycle During training, existing methods samples \mathbf{x}_t by interpolating noise ϵ_t and ground-truth \mathbf{x}_0 , which results in a certain level of data leak [Chen et al., 2022, Young et al., 2022]. Kolbeinsson and Mikolajczyk [2022] proposed recursive denoising, which performed T steps on each image progressively to use model’s predictions at previous steps. However, this extends the training length T times. Instead, in this work, for each image, the time step t is randomly sampled and the model’s prediction from the previous time step is recycled to replace ground-truth (Fig. 1):

$$\mathbf{x}_t = \sqrt{\bar{\alpha}_t}\mathbf{x}_{0, \theta}(\mathbf{x}_{t+1}, t+1, I) + \sqrt{1 - \bar{\alpha}_t}\epsilon_t, \quad (8)$$

$$\mathbf{x}_{t+1} = \sqrt{\bar{\alpha}_{t+1}}\mathbf{x}_0 + \sqrt{1 - \bar{\alpha}_{t+1}}\epsilon_{t+1}, \quad (9)$$

where $\mathbf{x}_{0, \theta}$ is the predicted segmentation mask from $t+1$ using ground-truth. ϵ_t and ϵ_{t+1} are two independently sampled noise. Gradient stop is applied to \mathbf{x}_{t+1} .

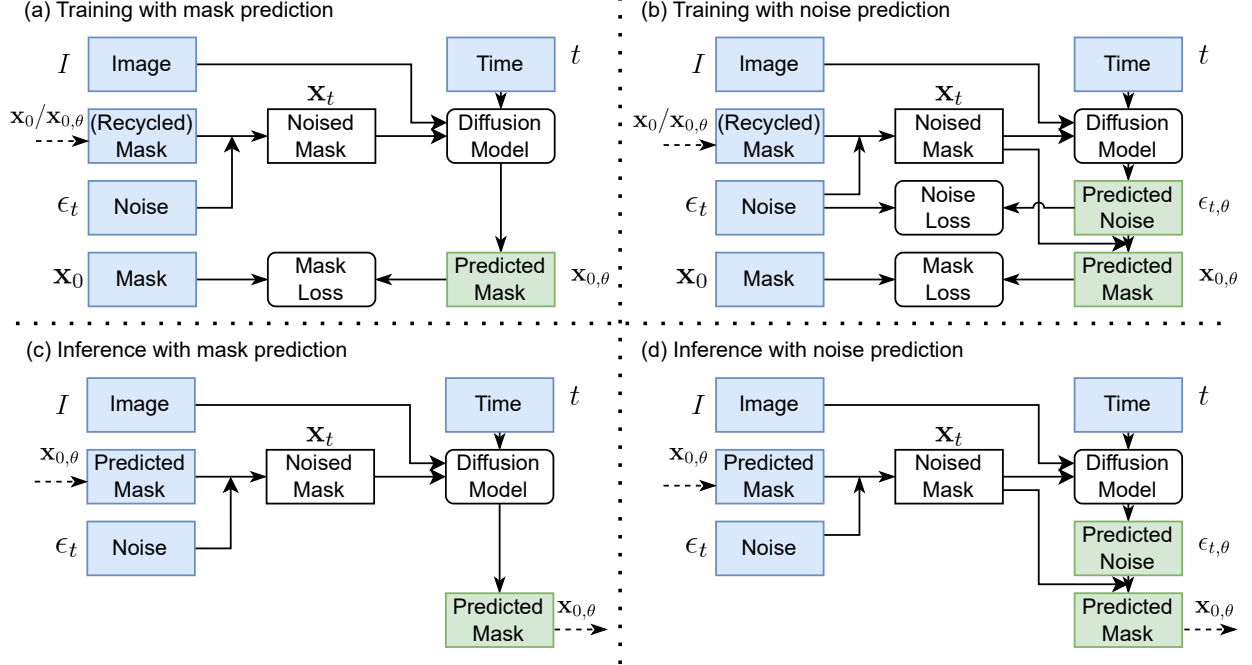


Figure 1: Illustration of training and inference with mask or noise prediction. For training (a, b), the noise-corrupted mask is calculated using the mask predicted at the previous time step when recycling. For inference (c, d), a random sampled noise is used for the first step as the predicted mask is not available.

4 Experiment Setting

4.1 Data

Prostate MR The data set¹ [Li et al., 2022] contains 589 T2-weighted image-mask pairs for 8 anatomical structures. The images were randomly split into non-overlapping training, validation, and test sets, with 411, 14, 164 images in each split, respectively. All images were normalised, resampled, and centre-cropped to an image size of $256 \times 256 \times 48$, with a voxel dimension of $0.75 \times 0.75 \times 2.5$ (mm).

Abdominal CT The data set² [Ji et al., 2022] provides 200 and 100 CT image-mask pairs for 15 abdominal organs in training and validation sets. The validation set was randomly split into non-overlapping validation and test sets, with 10 and 90 images, respectively. HU values were clipped to $[-991, 362]$ for all images. Images were then normalised, resampled and centre-cropped to an image size of $192 \times 128 \times 128$, with a voxel dimension of $1.5 \times 1.5 \times 5.0$ (mm).

4.2 Implementation Details

2D and 3D U-net variants were used. Images were sliced at the depth axis for 2D networks. U-nets have four layers with 32, 64, 128, and 256 channels, respectively. For diffusion-based models, noise-corrupted masks and images were concatenated along feature channels and time was encoded using sinusoidal positional embedding [Rombach et al., 2022]. Random rotation, translation and scaling were adopted for data augmentation during training. For DDPM, $T = 1000$ and a linear β schedule between 0.0001 and 0.02 was used. The variance $\sigma_t^2 = \frac{1-\bar{\alpha}_t-1}{1-\bar{\alpha}_t} \beta_t$. During training and inference, variances were resampled with 5 steps K by default. The segmentation-specific loss function is by default the sum of cross-entropy and foreground-only Dice loss. When predicting noise, the L_2 loss has a weight of 0.1 [Wu et al., 2022]. All models were trained with AdamW for 12500 steps and a warmup cosine learning rate schedule with a batch size of 8 and starting learning rate 10^{-5} . Hyper-parameter were configured empirically without extensive tuning.

¹<https://zenodo.org/record/7013610#.ZAKaXuzP2rM>

²<https://zenodo.org/record/7155725#.ZAKbe-zP2r0>

Models were trained once and checkpoints were saved at every 500 steps. Checkpoint having the best mean binary Dice score on validation set was used for testing. Binary Dice score (DS), normalised surface dice (NSD), 95% Hausdorff distance in mm (HD), and centroid distance in mm (CD), averaged over foreground classes, were reported. Paired Student’s t-tests were performed on Dice score to test statistical significance between model performance with $\alpha = 0.01$.

Experiments were performed using bfloat16 mixed precision on TPU v3-8, which has 16×8 GB device memory. Increasing batch size led to memory errors. Each training took around 11 hours and the evaluation took 5 hours, costing around 140 dollars per run. The JAX-based implementation code has been anonymised and released on <https://github.com/mathpluscode/ImgX-DiffSeg>.

5 Results

The performance of the proposed diffusion model is summarised in Table 1. Standard deviations were reported in Table 4. Within the same computing budget, the diffusion-based 3D model reached a Dice score of 0.830 and 0.801 which is competitive with 0.838 and 0.816 of its non-diffusion counterpart, for prostate MR and abdominal CT respectively. The difference, however, remains significant with $p < 0.001$. The Dice scores per class are visualised in Fig. 3 for both data sets. In general, all methods tend to perform better for large regions of interest (ROI), and there is a significant correlation (Spearman $r > 0.8$ and $p < 0.01$) between ROI (regions of interest) area and mean Dice score per ROI/class, indicating future improvement can be focused on addressing small ROIs. Example predictions were provided in Fig. 2, where the diffusion model maintained correct predictions while adjusting erroneous masks, visually comparable with results from U-net.

Ablation studies were performed on prostate MR data set to compare proposed modifications, as summarised in Table 2, including: 1) predicting mask instead of noise, 2) using Dice loss in addition to cross entropy, 3) recycling model prediction, 4) using five steps denoising process during training. Improvements in Dice score between 0.09 and 0.279 were observed for all modifications in 2D and 3D networks (all p-values < 0.001). The largest improvement was observed (an increase of 0.279 and 0.117 of Dice score for 2D and 3D networks respectively) when the model predicted segmentation masks instead of noise, indicating that noise prediction may require longer training time for convergence.

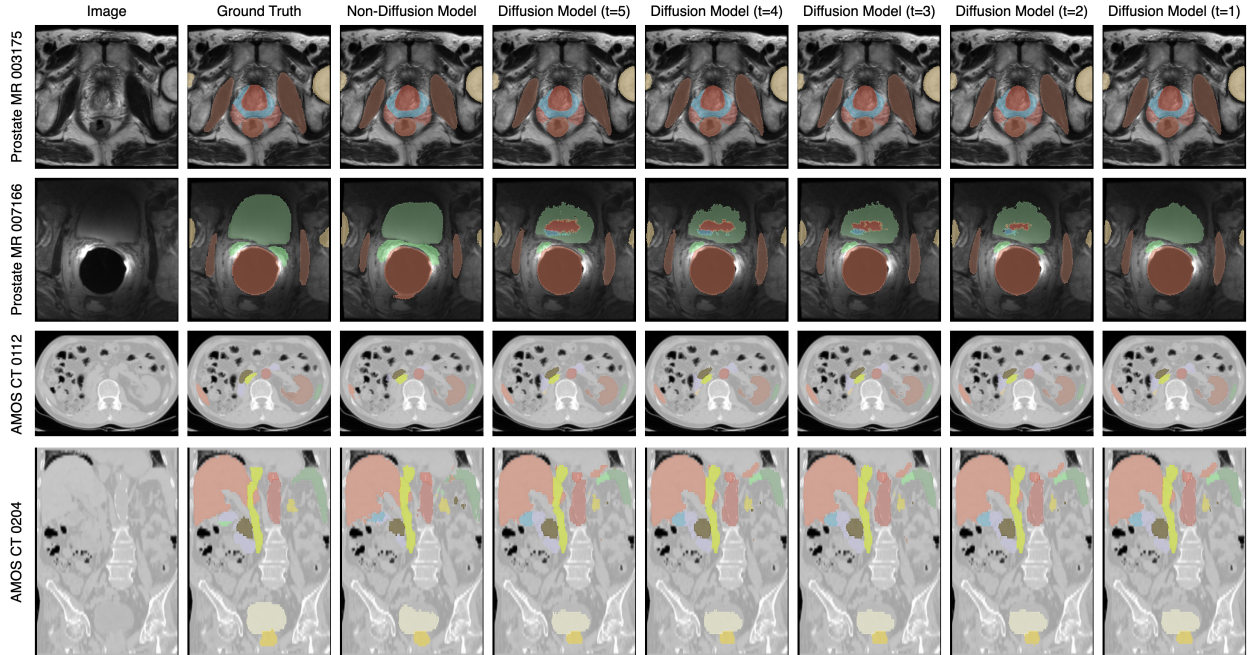


Figure 2: Comparison of non-diffusion models and diffusion models. Diffusion model maintained correct predictions while adjusting erroneous masks.

Table 1: Segmentation performance comparison between diffusion models and non-diffusion models for 2D and 3D networks. Y/N represents diffusion and non-diffusion models, respectively. Standard deviations are reported in Table 3.

Model	Diffusion	Prostate MR				Abdominal CT			
		DS \uparrow	NSD \uparrow	HD \downarrow	CD \downarrow	DS \uparrow	NSD \uparrow	HD \downarrow	CD \downarrow
2D	N	0.831	0.638	6.044	2.824	0.804	0.577	9.885	4.416
	Y	0.818	0.615	6.658	3.012	0.769	0.520	12.039	5.121
3D	N	0.838	0.648	5.197	2.675	0.816	0.596	9.091	4.275
	Y	0.830	0.626	5.424	3.009	0.801	0.540	9.125	4.836

Table 2: Ablation studies on prostate MR data set. All reported modifications led to statistically significant improvements (all p-values < 0.001). Standard deviations are reported in Table 4.

(a) Output indicates model predicting logits for mask or noise. (b) Dice indicates model using Dice loss or not, in addition to cross-entropy.

	Output	DS \uparrow	NSD \uparrow	HD \downarrow	CD \downarrow
2D	Noise	0.539	0.318	75.732	8.568
	Logits	0.818	0.615	6.658	3.012
3D	Noise	0.713	0.475	23.855	5.130
	Logits	0.830	0.626	5.424	3.009

	Dice	DS \uparrow	NSD \uparrow	HD \downarrow	CD \downarrow
2D	N	0.801	0.612	6.242	3.245
	Y	0.818	0.615	6.658	3.012
3D	N	0.812	0.613	5.463	3.354
	Y	0.830	0.626	5.424	3.009

(c) Recycle indicates model recycling predictions or using ground truth for noise-corrupted mask generation. (d) Steps are the number of time steps for the denoising process during training. Test always has 5 steps.

	Recycle	DS \uparrow	NSD \uparrow	HD \downarrow	CD \downarrow
2D	N	0.801	0.587	6.598	3.344
	Y	0.818	0.615	6.658	3.012
3D	N	0.815	0.587	5.485	3.337
	Y	0.830	0.626	5.424	3.009

	Steps	DS \uparrow	NSD \uparrow	HD \downarrow	CD \downarrow
2D	1000	0.801	0.586	6.798	3.305
	5	0.818	0.615	6.658	3.012
3D	1000	0.821	0.603	5.223	3.051
	5	0.830	0.626	5.424	3.009

6 Discussion

In this work, we developed the first denoising diffusion probabilistic model for 3D image multiclass segmentation. Compared to existing models, the proposed method applied segmentation-specific Dice loss and predicted segmentation masks in lieu of sampled errors. The method also reduced the number of timesteps from hundreds to five for both training and inference. These modifications bridged the gap between diffusion training and segmentation evaluation, which resulted in significant performance improvements compared to existing diffusion-based methods. However, the resulting model did not outperform the vanilla non-diffusion segmentation models trained in supervised learning, suggesting a limited benefit of the diffusion process in the studied application within a fixed computed budget. Future work would be further improvements for diffusion models.

Although the presented experimental results primarily demonstrated methodological development, the fact that these were obtained on two large clinical data sets represents a promising step towards real-world applications. Localising multiple anatomical structures in prostate MR images is key to MR-targeted biopsy, radiotherapy and tissue-preserving focal treatment for patients with urological diseases, while abdominal organ outlines can be directly used in planning gastroenterological procedures and hepatic surgery.

7 Acknowledgement

This work was supported by the Wellcome/EPSRC Centre for Interventional and Surgical Sciences (203145Z/16/Z), the EPSRC funded Centre for Doctoral Training in Intelligent, Integrated Imaging in Healthcare (i4Health) (EP/S021930/1), the EPSRC grant EP/T029404/1), the International Alliance for Cancer Early Detection, an alliance between Cancer Research UK [C28070/A30912; C73666/A31378], Canary Center at Stanford University, the University of Cambridge,

OHSU Knight Cancer Institute, University College London and the University of Manchester, and Cloud TPUs from Google's TPU Research Cloud (TRC).

References

- Xiaoxiao Li, Yuan Zhou, Nicha Dvornek, Muhan Zhang, Siyuan Gao, Juntang Zhuang, Dustin Scheinost, Lawrence H Staib, Pamela Ventola, and James S Duncan. Braingnn: Interpretable brain graph neural network for fmri analysis. *Medical Image Analysis*, 74:102233, 2021.
- Robin Strudel, Ricardo Garcia, Ivan Laptev, and Cordelia Schmid. Segmenter: Transformer for semantic segmentation. In *Proceedings of the IEEE/CVF international conference on computer vision*, pages 7262–7272, 2021.
- Veronika Cheplygina, Marleen de Bruijne, and Josien PW Pluim. Not-so-supervised: a survey of semi-supervised, multi-instance, and transfer learning in medical image analysis. *Medical image analysis*, 54:280–296, 2019.
- Yunguan Fu, Maria R Robu, Bongjin Koo, Crispin Schneider, Stijn van Laarhoven, Danail Stoyanov, Brian Davidson, Matthew J Clarkson, and Yipeng Hu. More unlabelled data or label more data? a study on semi-supervised laparoscopic image segmentation. *arXiv preprint arXiv:1908.08035*, 2019.
- Yiwen Li, Yunguan Fu, Iani Gayo, Qianye Yang, Zhe Min, Shaheer Saeed, Wen Yan, Yipei Wang, J Alison Noble, Mark Emberton, et al. Prototypical few-shot segmentation for cross-institution male pelvic structures with spatial registration. *arXiv preprint arXiv:2209.05160*, 2022.
- Olaf Ronneberger, Philipp Fischer, and Thomas Brox. U-net: Convolutional networks for biomedical image segmentation. In *Medical Image Computing and Computer-Assisted Intervention—MICCAI 2015: 18th International Conference, Munich, Germany, October 5–9, 2015, Proceedings, Part III* 18, pages 234–241. Springer, 2015.
- Yuanfeng Ji, Haotian Bai, Jie Yang, Chongjian Ge, Ye Zhu, Ruimao Zhang, Zhen Li, Lingyan Zhang, Wanling Ma, Xiang Wan, et al. Amos: A large-scale abdominal multi-organ benchmark for versatile medical image segmentation. *arXiv preprint arXiv:2206.08023*, 2022.
- Jonathan Ho, Ajay Jain, and Pieter Abbeel. Denoising diffusion probabilistic models. *Advances in Neural Information Processing Systems*, 33:6840–6851, 2020.
- Prafulla Dhariwal and Alexander Nichol. Diffusion models beat gans on image synthesis. *Advances in Neural Information Processing Systems*, 34:8780–8794, 2021.
- Jonathan Ho and Tim Salimans. Classifier-free diffusion guidance. *arXiv preprint arXiv:2207.12598*, 2022.
- Tomer Amit, Eliya Nachmani, Tal Shaharabany, and Lior Wolf. Segdiff: Image segmentation with diffusion probabilistic models. *arXiv preprint arXiv:2112.00390*, 2021.
- Benedikt Kolbeinsson and Krystian Mikolajczyk. Multi-class segmentation from aerial views using recursive noise diffusion. *arXiv preprint arXiv:2212.00787*, 2022.
- Julia Wolleb, Robin Sandkühler, Florentin Bieder, Philippe Valmaggia, and Philippe C Cattin. Diffusion models for implicit image segmentation ensembles. In *International Conference on Medical Imaging with Deep Learning*, pages 1336–1348. PMLR, 2022.
- Junde Wu, Huihui Fang, Yu Zhang, Yehui Yang, and Yanwu Xu. Medsegdiff: Medical image segmentation with diffusion probabilistic model. *arXiv preprint arXiv:2211.00611*, 2022.
- Ting Chen, Lala Li, Saurabh Saxena, Geoffrey Hinton, and David J Fleet. A generalist framework for panoptic segmentation of images and videos. *arXiv preprint arXiv:2210.06366*, 2022.
- Sean I Young, Adrian V Dalca, Enzo Ferrante, Polina Golland, Bruce Fischl, and Juan Eugenio Iglesias. Sud: Supervision by denoising for medical image segmentation. *arXiv preprint arXiv:2202.02952*, 2022.
- Alexander Quinn Nichol and Prafulla Dhariwal. Improved denoising diffusion probabilistic models. In *International Conference on Machine Learning*, pages 8162–8171. PMLR, 2021.
- Jascha Sohl-Dickstein, Eric Weiss, Niru Maheswaranathan, and Surya Ganguli. Deep unsupervised learning using nonequilibrium thermodynamics. In *International Conference on Machine Learning*, pages 2256–2265. PMLR, 2015.
- Alec Radford, Jong Wook Kim, Chris Hallacy, Aditya Ramesh, Gabriel Goh, Sandhini Agarwal, Girish Sastry, Amanda Askell, Pamela Mishkin, Jack Clark, et al. Learning transferable visual models from natural language supervision. In *International conference on machine learning*, pages 8748–8763. PMLR, 2021.
- Hazrat Ali, Shafaq Murad, and Zubair Shah. Spot the fake lungs: Generating synthetic medical images using neural diffusion models. In *Artificial Intelligence and Cognitive Science: 30th Irish Conference, AICS 2022, Munster, Ireland, December 8–9, 2022, Revised Selected Papers*, pages 32–39. Springer, 2023.
- Walter HL Pinaya, Petru-Daniel Tudosiu, Jessica Dafflon, Pedro F da Costa, Virginia Fernandez, Parashkev Nachev, Sebastien Ourselin, and M Jorge Cardoso. Brain imaging generation with latent diffusion models. *arXiv preprint arXiv:2209.07162*, 2022.

- Boah Kim and Jong Chul Ye. Diffusion deformable model for 4d temporal medical image generation. In *Medical Image Computing and Computer Assisted Intervention—MICCAI 2022: 25th International Conference, Singapore, September 18–22, 2022, Proceedings, Part I*, pages 539–548. Springer, 2022.
- Shaheer U. Saeed, Tom Syer, Wen Yan, Qianye Yang, Mark Emberton, Shonit Punwani, Matthew J. Clarkson, Dean C. Barratt, and Yipeng Hu. Bi-parametric prostate mr image synthesis using pathology and sequence-conditioned stable diffusion. *arXiv preprint arXiv:2303.02094*, 2023.
- Firas Khader, Gustav Mueller-Franzes, Soroosh Tayebi Arasteh, Tianyu Han, Christoph Haarbuerger, Maximilian Schulze-Hagen, Philipp Schad, Sandy Engelhardt, Bettina Baessler, Sebastian Foersch, et al. Medical diffusion–denoising diffusion probabilistic models for 3d medical image generation. *arXiv preprint arXiv:2211.03364*, 2022.
- Dmitry Baranchuk, Ivan Rubachev, Andrey Voynov, Valentin Khrulkov, and Artem Babenko. Label-efficient semantic segmentation with diffusion models. *arXiv preprint arXiv:2112.03126*, 2021.
- Diederik Kingma, Tim Salimans, Ben Poole, and Jonathan Ho. Variational diffusion models. *Advances in neural information processing systems*, 34:21696–21707, 2021.
- Robin Rombach, Andreas Blattmann, Dominik Lorenz, Patrick Esser, and Björn Ommer. High-resolution image synthesis with latent diffusion models. In *Proceedings of the IEEE/CVF Conference on Computer Vision and Pattern Recognition*, pages 10684–10695, 2022.

Appendix



Figure 3: Mean Dice score per class on prostate MR (top) and abdominal CT (bottom) data set. The average proportion of the class is indicated beside names. The Spearman correlations between ROI proportion in volume and mean Dice score are 0.93, 0.86, 0.83, and 0.86 for 2D diffusion, 3D diffusion, 2D non-diffusion, and 3D non-diffusion models on prostate MR, and 0.85, 0.86, 0.81, 0.81 on abdominal CT, respectively. Correlations are all significant with $\alpha = 0.01$.

Table 3: Segmentation performance comparison between diffusion models and non-diffusion models for 2D and 3D networks. Y/N represents diffusion and non-diffusion models, respectively. Binary Dice score (DS), normalised surface dice (NSD), 95% Hausdorff distance in mm (HD), and centroid distance in mm (CD), averaged over foreground classes, were reported together with standard deviations.

(a) Prostate MR

Model	Diffusion	DS \uparrow	NSD \uparrow	HD \downarrow	CD \downarrow
2D	N	0.831 (0.098)	0.638 (0.113)	6.044 (1.031)	2.824 (1.239)
	Y	0.818 (0.102)	0.615 (0.118)	6.658 (0.839)	3.012 (1.174)
3D	N	0.838 (0.088)	0.648 (0.110)	5.197 (1.184)	2.675 (0.927)
	Y	0.830 (0.094)	0.626 (0.112)	5.424 (1.176)	3.009 (1.165)

(b) Abdominal CT

Model	Diffusion	DS \uparrow	NSD \uparrow	HD \downarrow	CD \downarrow
2D	N	0.804 (0.109)	0.577 (0.082)	9.885 (2.587)	4.416 (1.914)
	Y	0.769 (0.127)	0.520 (0.091)	12.039 (2.932)	5.121 (2.102)
3D	N	0.816 (0.100)	0.596 (0.084)	9.091 (2.475)	4.275 (1.870)
	Y	0.801 (0.109)	0.540 (0.095)	9.125 (2.564)	4.836 (2.273)

Table 4: Ablation studies of proposed methods on prostate MR data set. All modifications led to significant improvements.

(a) Output indicates model predicting logits for mask or noise.

Model	Output	DS \uparrow	NSD \uparrow	HD \downarrow	CD \downarrow
2D	Noise	0.539 (0.161)	0.318 (0.082)	75.732 (10.585)	8.568 (3.279)
	Logits	0.818 (0.102)	0.615 (0.118)	6.658 (0.839)	3.012 (1.174)
3D	Noise	0.713 (0.129)	0.475 (0.089)	23.855 (4.977)	5.130 (1.205)
	Logits	0.830 (0.094)	0.626 (0.112)	5.424 (1.176)	3.009 (1.165)

(b) Dice indicates model using Dice loss or not, in addition to cross-entropy.

Model	Dice	DS \uparrow	NSD \uparrow	HD \downarrow	CD \downarrow
2D	N	0.801 (0.125)	0.612 (0.129)	6.242 (0.752)	3.245 (1.362)
	Y	0.818 (0.102)	0.615 (0.118)	6.658 (0.839)	3.012 (1.174)
3D	N	0.812 (0.111)	0.613 (0.121)	5.463 (1.051)	3.354 (1.303)
	Y	0.830 (0.094)	0.626 (0.112)	5.424 (1.176)	3.009 (1.165)

(c) Recycle indicates model recycling predictions or using ground truth for noisy mask generation.

Model	Recycle	mDS \uparrow	mNSD \uparrow	mHD \downarrow	mCD \downarrow
2D	N	0.801 (0.112)	0.587 (0.121)	6.598 (0.828)	3.344 (1.332)
	Y	0.818 (0.102)	0.615 (0.118)	6.658 (0.839)	3.012 (1.174)
3D	N	0.815 (0.095)	0.587 (0.105)	5.485 (1.069)	3.337 (1.061)
	Y	0.830 (0.094)	0.626 (0.112)	5.424 (1.176)	3.009 (1.165)

(d) Steps are the number of time steps for the denoising process during training. Test always has 5 steps.

Model	Steps	DS \uparrow	NSD \uparrow	HD \downarrow	CD \downarrow
2D	1000	0.801 (0.111)	0.586 (0.124)	6.798 (0.846)	3.305 (1.193)
	5	0.818 (0.102)	0.615 (0.118)	6.658 (0.839)	3.012 (1.174)
3D	1000	0.821 (0.095)	0.603 (0.107)	5.223 (1.064)	3.051 (1.111)
	5	0.830 (0.094)	0.626 (0.112)	5.424 (1.176)	3.009 (1.165)